
This is an electronic reprint of the original article.
This reprint may differ from the original in pagination and typographic detail.

Seidu, Azimatu; Dvorak, Marc; Rinke, Patrick; Li, Jingrui
Atomic and electronic structure of cesium lead triiodide surfaces

Published in:
Journal of Chemical Physics

DOI:
[10.1063/5.0035448](https://doi.org/10.1063/5.0035448)

Published: 21/02/2021

Document Version
Publisher's PDF, also known as Version of record

Published under the following license:
CC BY

Please cite the original version:
Seidu, A., Dvorak, M., Rinke, P., & Li, J. (2021). Atomic and electronic structure of cesium lead triiodide surfaces. *Journal of Chemical Physics*, 154(7), Article 074712. <https://doi.org/10.1063/5.0035448>

This material is protected by copyright and other intellectual property rights, and duplication or sale of all or part of any of the repository collections is not permitted, except that material may be duplicated by you for your research use or educational purposes in electronic or print form. You must obtain permission for any other use. Electronic or print copies may not be offered, whether for sale or otherwise to anyone who is not an authorised user.

Atomic and electronic structure of cesium lead triiodide surfaces

Cite as: J. Chem. Phys. **154**, 074712 (2021); <https://doi.org/10.1063/5.0035448>

Submitted: 29 October 2020 . Accepted: 24 January 2021 . Published Online: 19 February 2021

 Azimatu Seidu,  Marc Dvorak,  Patrick Rinke, and  Jingrui Li



View Online



Export Citation



CrossMark

ARTICLES YOU MAY BE INTERESTED IN

[Uncertainty estimation for molecular dynamics and sampling](#)

The Journal of Chemical Physics **154**, 074102 (2021); <https://doi.org/10.1063/5.0036522>

[Effects of interaction strength of associating groups on linear and star polymer dynamics](#)

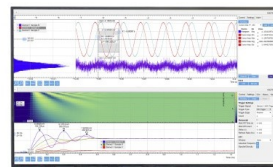
The Journal of Chemical Physics **154**, 074903 (2021); <https://doi.org/10.1063/5.0038097>

[The Devil's Triangle of Kohn-Sham density functional theory and excited states](#)

The Journal of Chemical Physics **154**, 074106 (2021); <https://doi.org/10.1063/5.0035446>

Challenge us.

What are your needs for
periodic signal detection?



Zurich
Instruments

Atomic and electronic structure of cesium lead triiodide surfaces

Cite as: *J. Chem. Phys.* **154**, 074712 (2021); doi: [10.1063/5.0035448](https://doi.org/10.1063/5.0035448)

Submitted: 29 October 2020 • Accepted: 24 January 2021 •

Published Online: 19 February 2021



View Online



Export Citation



CrossMark

Azimatu Seidu,^{1,a)}  Marc Dvorak,¹  Patrick Rinke,¹  and Jingrui Li² 

AFFILIATIONS

¹Department of Applied Physics, Aalto University, FI-00076 Aalto, Finland

²Electronic Materials Research Laboratory, Key Laboratory of the Ministry of Education and International Center for Dielectric Research, School of Electronic Science and Engineering, Xi'an Jiaotong University, Xi'an 710049, China

^{a)} Author to whom correspondence should be addressed: azimatu.seidu@aalto.fi

ABSTRACT

The (001) surface of the emerging photovoltaic material cesium lead triiodide (CsPbI_3) is studied. Using first-principles methods, we investigate the atomic and electronic structure of cubic (α) and orthorhombic (γ) CsPbI_3 . For both phases, we find that CsI-termination is more stable than PbI_2 -termination. For the CsI-terminated surface, we then compute and analyze the surface phase diagram. We observe that surfaces with added or removed units of nonpolar CsI and PbI_2 are most stable. The corresponding band structures reveal that the α phase exhibits surface states that derive from the conduction band. The surface reconstructions do not introduce new states in the bandgap of CsPbI_3 , but for the α phase, we find additional surface states at the conduction band edge.

© 2021 Author(s). All article content, except where otherwise noted, is licensed under a Creative Commons Attribution (CC BY) license (<http://creativecommons.org/licenses/by/4.0/>). <https://doi.org/10.1063/5.0035448>

I. INTRODUCTION

In recent years, perovskite solar cells (PSCs) have generated increased attention within the photovoltaic community. The most common PSC photoabsorbers are hybrid organic-inorganic halide perovskites (HPs) with an ABX_3 structure, where A is an (organic) monovalent cation, B is either Pb or Sn, and X is a halogen. Among the HPs, the most widely studied materials are methylammonium (MA) lead iodide ($\text{CH}_3\text{NH}_3\text{PbI}_3$ or MAPbI_3) and formamidinium (FA) lead iodide [$\text{HC}(\text{NH}_2)_2\text{PbI}_3$ or FAPbI_3]. HPs are the most promising materials for next-generation photovoltaic technologies, as reflected by their rapidly rising power conversion efficiency (PCE): It reached $\sim 25\%$ only seven years after the invention of the state-of-the-art PSC architecture in 2012 (PCE $\sim 10\%$).^{2,3} HPs are also promising for light emitting diodes, lasers, and photodetectors.^{4–6} Their outstanding properties for optoelectronic applications include optimal bandgaps, excellent absorption in the visible range of the solar spectrum, exceptional transport properties for both electrons and holes, flexibility of composition engineering, and low cost in both materials and fabrication.^{7–12}

Despite the rapid PCE improvement in the laboratory, stability issues limit the development and commercialization of HPs for real photovoltaic applications. Especially, the organic components in hybrid perovskites are susceptible to ambient conditions such as moisture, oxygen, and heat, and exposure leads to rapid performance degradation.^{13–19} Several approaches have been proposed to solve these pressing stability problems, including surface protection with organic long-chain ligands,^{20–22} synthesis of quasi-two-dimensional perovskites,^{23–28} protective coating with inorganic semiconductors or insulators,^{29–32} and A-site substitution with smaller monovalent ions.^{18,33–39}

In the context of A-site substitutions, the all-inorganic perovskite CsPbI_3 and its mixed-halide derivatives have emerged as a promising alternative to the hybrid MA- and FA-based perovskites. CsPbI_3 has a similar structure and slightly closer Pb-I packing and higher thermal and chemical stabilities than MAPbI_3 and FAPbI_3 .^{11,40} The latest PCE of CsPbI_3 -based PSCs has already reached 18%,⁴¹ but more material design and device engineering are needed to increase the conversion efficiency and the operational stability. This applies to several aspects, such as morphology

control of the HP thin films, interface engineering between CsPbI₃ and interlayer materials, and the passivation of intrinsic defects at the interfaces and grain boundaries, which act as nonradiative recombination centers, thus degrading the device efficiency. A comprehensive understanding of the atomic and electronic structure of CsPbI₃ surfaces would advance its development as a PSC photoabsorber. The surfaces of MA- and FA-based perovskites have been investigated theoretically^{42–45} and experimentally.^{46–51} For CsPbI₃, however, we are only aware of bulk defect studies.^{52–55} The surfaces and interfaces of CsPbI₃ have not yet been considered.

In this work, we present first-principles density functional theory (DFT) calculations for the reconstructed surfaces of the photovoltaic-active α (cubic) and γ (orthorhombic) phases of CsPbI₃. Starting from the pristine (clean) surface models with CsI- and PbI₂-terminations (denoted by CsI-T and PbI₂-T, respectively), constituent elements (Cs, Pb, and I) as well as their complexes (CsI, PbI, and PbI₂) were added to or removed from the surface. The thermodynamic stability of these surface models will be investigated with surface phase diagram (SPD) analysis for different chemical environments by means of *ab initio* thermodynamics.^{56–58} For the stable surface models, we calculated their electronic structure and elucidated changes in their electronic properties in comparison to the clean surfaces.

The remainder of this paper is organized as follows: In Sec. II, we briefly outline the computational details of our DFT calculations and summarize the thermodynamic constraints for the growth of bulk CsPbI₃ as well as the CsI-T and PbI₂-T surfaces. In Sec. III, we first analyze the stability of the clean-surface models (CsI-T and Pb₂-T) and the reconstructed models with missing- and add-atoms (and their complexes). We then discuss changes in crystal structures due to missing- and add-atoms with focus on their stability and their atomic and electronic structures. Finally, we conclude with a summary in Sec. V.

II. COMPUTATIONAL DETAILS

All DFT calculations were performed using the Perdew–Burke–Ernzerhof exchange–correlation functional for solids (PBEsol)⁵⁹ implemented in the all-electron numeric-atom-centered orbital code FHI-AIMS.^{60–62} We chose PBEsol because it describes the lattice constants of CsPbI₃ well at moderate computational cost.^{63,64} Scalar relativistic effects were included by means of the zeroth-order regular approximation.⁶⁵ We used standard FHI-AIMS tier two basis sets for all calculations, in combination with a Γ -centered $4 \times 4 \times 4$ and a $4 \times 4 \times 1$ k -point mesh for the bulk materials and the surface calculations with a slab model, respectively. The bulk structures were optimized with the analytical stress tensor.⁶⁶ For the slab models, we fixed the lattice constants and all atomic positions except for atoms in the top and bottom CsPbI₃ units (the surface atoms). Surface-dipole correction⁶⁷ was used in all surface calculations.

A. Structural optimization

1. Bulk and surface structures

In this work, we considered two experimentally accessible photovoltaic-active perovskite phases of CsPbI₃: the α (cubic) phase with space group Pm $\bar{3}$ m and the γ (orthorhombic) phase with

space group Pnma. For each phase, we constructed and optimized a $2 \times 2 \times 2$ bulk supercell with DFT (structures shown in Fig. 1). The lattice parameters of our optimized α phase are $a = b = c = 12.47$ Å and $\alpha = \beta = \gamma = 90^\circ$. For the γ phase, the lattice parameters are $a = b = 12.21$ Å, $c = 12.35$ Å, and $\alpha = \beta = 90^\circ$, $\gamma = 85.8^\circ$.

For each phase, we constructed the surface models by inserting a vacuum region in the [001] direction of the investigated system. With a 30 Å vacuum thickness and the inclusion of surface-dipole correction,⁶⁷ we minimized the interaction between neighboring slabs. In this work, we focused on the (001) surfaces, which are the major facet of halide perovskites^{42,43,68} and the most relevant surfaces of CsPbI₃. We carried out DFT calculations for CsPbI₃ surfaces with symmetric slab models for CsI-T and PbI₂-T surfaces. As depicted in Fig. 2, the CsI-T surface model consists of five CsI and four PbI₂ layers alternatively stacked along the [001] direction. Similarly, the PbI₂-T surface model has five PbI₂ and four CsI alternating layers. To remove quantum confinement effects from the band structure, we performed slab-model calculations with up to 5 additional CsPbI₃ layers before and after relaxation.

For both CsI-T and PbI₂-T surface models, we studied different missing- and add-atom reconstructions. The missing- and add-atoms are labeled as v_X and i_X , respectively, with X indicating the atoms or their complexes. All add-atoms and their complexes were added to the surfaces, while missing-atoms were removed from the topmost layers containing those atoms. For instance, v_{Cs} , v_I , and v_{CsI} of CsI-T surfaces were constructed by removing atoms from the topmost CsI layer, while v_{Pb} , v_{PbI} , and v_{PbI_2} indicate the removal of atoms from the PbI₂ layer below the topmost CsI layer.

The 2×2 surface unit cell allows us to study 26 reconstructed surface models each for CsI-T and PbI₂-T. In detail, these amount to 13 missing-atom or missing-complex models and 13 add-atom or add-complex structures, as listed in Table I. For double missing- and add-atoms (i.e., v_{2X} and i_{2X}), we considered both line and diagonal options (i.e., removing two iodine atoms along the [100] or [110] directions for v_{2I}). We found no significant total-energy differences between these two modes. Hence, we only present results from the diagonal modes in this paper.

In pursuit of open materials science,⁶⁹ we made the results of all relevant calculations available on the Novel Materials Discovery (NOMAD) repository.⁷⁰

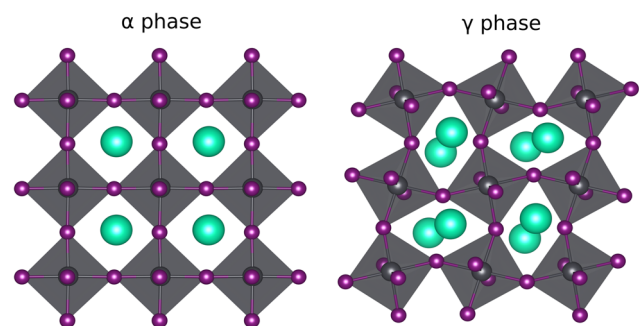


FIG. 1. Bulk crystal structures of the α (cubic) and the γ (orthorhombic) phases of CsPbI₃. Cs, Pb, and I are colored in green, black, and purple, respectively. The PbI₆ octahedra are colored in dark gray.

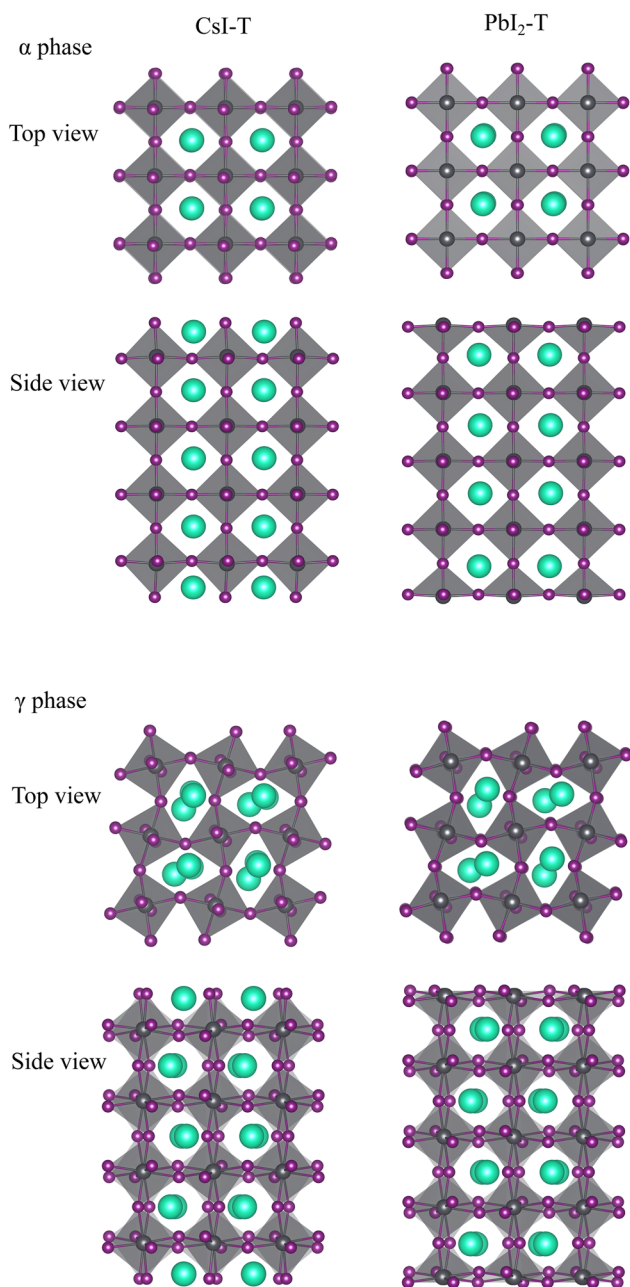


FIG. 2. Relaxed CsI-T and PbI₂-T clean-surface models of the α and the γ phases. Depicted are the CsI-T on the left and the PbI₂-T termination on the right.

B. Grand potential analysis

For a system in contact with a particle reservoir and neglecting finite temperature contributions, the thermodynamic stability of a structure is obtained from the grand potential, Ω ,

$$\Omega \approx E - \sum_i x_i \mu_i. \quad (1)$$

TABLE I. CsI-T and PbI₂-T surface models in the α and the γ phases.

CsI-T		PbI ₂ -T	
V _{Cs}	i _{Cs}	V _{Cs}	i _{Cs}
V _{2Cs}	i _{2Cs}	V _{2Cs}	i _{2Cs}
V _{4Cs}	i ₁	V ₁	i ₁
V ₁	i _{2I}	V _{2I}	i _{2I}
V _{2I}	i _{Pb}	V _{Pb}	i _{Pb}
V _{Pb}	i _{2Pb}	V _{2Pb}	i _{2Pb}
V _{2Pb}	i _{CsI}	V _{4Pb}	i _{CsI}
V _{CsI}	i _{2CsI}	V _{CsI}	i _{2CsI}
V _{2CsI}	i _{4CsI}	V _{2CsI}	i _{PbI}
V _{PbI}	i _{PbI}	V _{PbI}	i _{2PbI}
V _{2PbI}	i _{2PbI}	V _{2PbI}	i _{PbI₂}
V _{PbI₂}	i _{PbI₂}	V _{PbI₂}	i _{2PbI₂}
V _{2PbI₂}	i _{2PbI₂}	V _{2PbI₂}	i _{4PbI₂}

Here, μ_i is the chemical potential of species i and x_i is the number of atoms of this species in the structure. The sum over i runs over all elements in the compound. The relative stability between two systems in contact with the same particle reservoir is determined by differences in Ω with $\Omega^A < \Omega^B$ indicating that phase A is more stable than phase B. A special case of Ω is when a system is in contact with its constituent species in their most stable phase. This defines the standard formation energy, which is denoted by ΔH hereafter,

$$\Delta H = E - \sum_i x_i \mu_i^\ominus. \quad (2)$$

Here, μ_i^\ominus indicates the chemical potential of species i in its most stable form. The thermodynamic stability condition $\Delta H < 0$ states that the system's total energy must be lower than the sum of its constituents' chemical potentials, each in their most stable phase.

The chemical potentials μ_i are set by environmental conditions. We apply a simple transformation to the chemical potentials,

$$\Delta\mu_i = \mu_i - \mu_i^\ominus, \quad (3)$$

to introduce the parameter $\Delta\mu_i$. $\Delta\mu_i$ is the change in the chemical potential away from its value in the element's most stable phase, μ_i^\ominus . $\Delta\mu_i$ represent environmental growth conditions and are a convenient parameter to vary in order to map phase diagrams. The grand potential can be rewritten as

$$\Omega = E - \sum_i x_i \mu_i^\ominus - \sum_i x_i \Delta\mu_i. \quad (4)$$

The relative stability condition between phases A and B is then

$$\Omega^A < \Omega^B, \quad (5)$$

which can be rearranged as

$$\left(E^A - \sum_i x_i^A \mu_i^\ominus \right) - \left(E^B - \sum_i x_i^B \mu_i^\ominus \right) < \sum_i (x_i^A - x_i^B) \Delta\mu_i.$$

We recognize ΔH for phases A and B ,

$$\Delta H^A - \Delta H^B < \sum_i (x_i^A - x_i^B) \Delta \mu_i. \quad (6)$$

The inequality given in Eq. (6) is the basis for the phase diagram, including the SPDs in this work. We calculate ΔH using the DFT total energy of the surface for E and the DFT total energy per species unit for μ_i^\ominus . For the specific case of a surface formation energy, ΔH reduces to

$$\Delta H^{\text{surf}} = E^{\text{surf}} - E^{\text{bulk}} - E^{\text{ads}} \quad (7)$$

for surface total energy E^{surf} , bulk total energy E^{bulk} , and the total energy of any adsorbants E^{ads} . With the various total energies tabulated from DFT calculations, we plot an SPD based on the inequalities in Eq. (6) as a function of the parameters $\Delta \mu_i$.

C. Thermodynamic constraints for stable CsPbI₃ bulk and surfaces

We first consider conditions for stable CsPbI₃ in the bulk. In order to avoid the formation of elementary Cs, Pb, and I as well as bulk CsI and PbI₂, the region of the phase diagram for stable CsPbI₃ is determined by the inequalities,

$$\begin{aligned} \Delta H(\text{CsPbI}_3) &\leq \Delta \mu_{\text{Cs}} \leq 0, \\ \Delta H(\text{CsPbI}_3) &\leq \Delta \mu_{\text{Pb}} \leq 0, \\ \Delta H(\text{CsPbI}_3) &\leq 3\Delta \mu_{\text{I}} \leq 0 \end{aligned} \quad (8)$$

and

$$\begin{aligned} \Delta H(\text{CsPbI}_3) &\leq \Delta \mu_{\text{Cs}} + \Delta \mu_{\text{Pb}} + 3\Delta \mu_{\text{I}}, \\ \Delta \mu_{\text{Cs}} + \Delta \mu_{\text{I}} &\leq \Delta H(\text{CsI}), \\ \Delta \mu_{\text{Pb}} + 2\Delta \mu_{\text{I}} &\leq \Delta H(\text{PbI}_2). \end{aligned} \quad (9)$$

The inequalities in Eq. (9) can be rearranged as

$$\begin{aligned} \Delta H(\text{CsPbI}_3) &\leq \Delta \mu_{\text{Cs}} + \Delta \mu_{\text{Pb}} + 3\Delta \mu_{\text{I}}, \\ \Delta H(\text{CsPbI}_3) - \Delta H(\text{CsI}) &\leq \Delta \mu_{\text{Pb}} + 2\Delta \mu_{\text{I}} \leq \Delta H(\text{PbI}_2), \\ \Delta H(\text{CsPbI}_3) - \Delta H(\text{PbI}_2) &\leq \Delta \mu_{\text{Cs}} + \Delta \mu_{\text{I}} \leq \Delta H(\text{CsI}). \end{aligned} \quad (10)$$

μ_{Cs}^\ominus , μ_{Pb}^\ominus , and μ_{I}^\ominus are calculated for the stable structures of Cs (I43m), Pb (P6₃/mmc), and I (I₂ molecule). Equations (8) and (10) are the conditions for stable CsPbI₃. Formation energies ΔH for Eqs. (8) and (10) are calculated with DFT. Varying the three parameters $\Delta \mu_{\text{Cs}}$, $\Delta \mu_{\text{Pb}}$, and $\Delta \mu_{\text{I}}$ maps the bulk stability region.

To compare the stability of two surfaces, we solve Eq. (6) to obtain the SPDs. Equation (6) is a condition for surface stability in addition to Eqs. (8) and (10), which are only for the bulk. The bulk and surface are not in isolation from each other. For this reason, the final surface stability is determined by overlaying the SPD on the bulk stability region. We consider the overlap of the stable bulk region with the SPD to be the predictor of a viable bulk and surface together.

III. RESULTS AND DISCUSSION

In this section, we present the results from our thermodynamic analysis, compare the stability of our surface termination models (CsI-T vs PbI₂-T), and analyze the most relevant terminations using SPDs. We conclude the section with the electronic properties of the bulk and most relevant reconstructed surface models.

A. Thermodynamic stability limits for CsPbI₃ bulk and surface terminations

The PBEsol-calculated formation energies of bulk CsI, PbI₂, α -CsPbI₃, and γ -CsPbI₃ are -3.40 , -2.47 , -5.89 , and -6.02 eV, respectively. From Eq. (10), the thermodynamic growth limits for bulk CsPbI₃ in the α and the γ phases at $\Delta \mu_{\text{Cs}} = 0$ then are

$$\begin{aligned} -2.49 \text{ eV} &\leq \Delta \mu_{\text{Pb}} + 2\Delta \mu_{\text{I}} \leq -2.47 \text{ eV} \quad \text{for } \alpha, \\ -2.62 \text{ eV} &\leq \Delta \mu_{\text{Pb}} + 2\Delta \mu_{\text{I}} \leq -2.47 \text{ eV} \quad \text{for } \gamma. \end{aligned} \quad (11)$$

Similarly, the growth limits for bulk CsPbI₃ at $\Delta \mu_{\text{Pb}} = 0$ in the α and the γ phases are

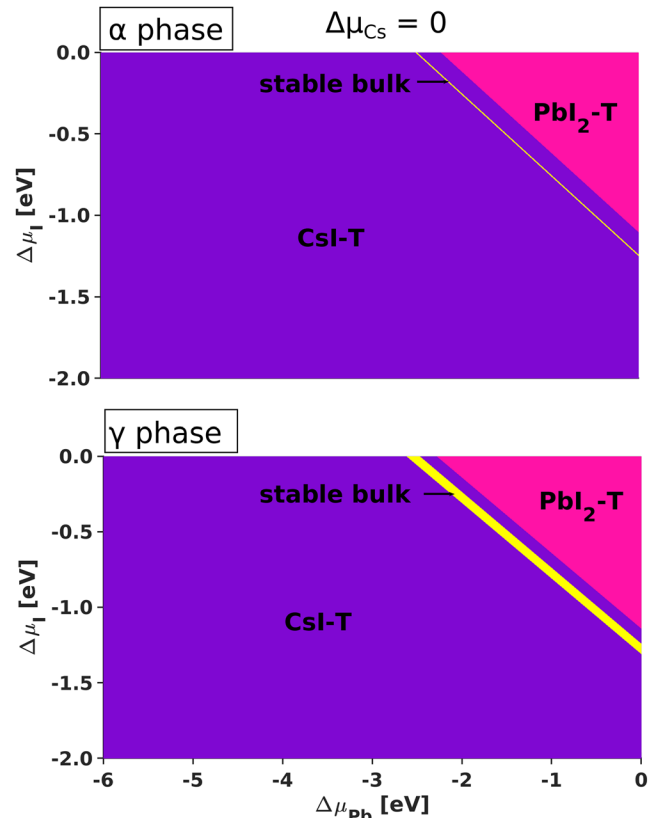


FIG. 3. Thermodynamic growth limit for CsI-T and PbI₂-T surfaces in the α and the γ phases at $\Delta \mu_{\text{Cs}} = 0$. The yellow shaded regions depict the thermodynamically stable range for the growth of bulk CsPbI₃.

$$\begin{aligned} -3.42 \text{ eV} &\leq \Delta\mu_{\text{Cs}} + \Delta\mu_{\text{I}} \leq -3.40 \text{ eV} && \text{for } \alpha, \\ -3.55 \text{ eV} &\leq \Delta\mu_{\text{Cs}} + \Delta\mu_{\text{I}} \leq -3.40 \text{ eV} && \text{for } \gamma. \end{aligned} \quad (12)$$

The small difference between the left and the right values of these inequalities indicates the narrow stability region of bulk CsPbI₃. The stability window in the α phase is especially small, only ~ 0.02 eV. For each phase, the width of this region equals the energy required for CsPbI₃ to decompose into CsI and PbI₂. Therefore, the narrow energy range for the growth of bulk CsPbI₃ reflects the instability and ease of dissociation of CsPbI₃ into CsI and PbI₂, as alluded to in Sec. I.

Figure 3 depicts the SPDs for the CsI-T and PbI₂-T clean surfaces in the α and the γ phases at $\Delta\mu_{\text{Cs}} = 0$. The stable bulk region is represented with the yellow shading. The CsI-T and PbI₂-T surfaces are stable in different regions. Since the CsI-T surface intersects

the stable bulk region, we consider it more stable in conditions for bulk growth. Additionally, we observe stable CsI-T surfaces across a wider range of $\Delta\mu_k$ ($k = \text{Cs, Pb, I}$) than PbI₂-T surfaces. The results of Fig. 3 are similar to the findings of previous theoretical studies for MAPbI₃^{42,43,71,72} on the stability of methylammonium-iodide terminated over PbI₂-T surfaces. Our discussions will therefore focus on CsI-T surfaces from here on. The data for PbI₂-T surfaces including the relaxed surface-reconstruction structures and the SPDs are given in the [supplementary material](#).

1. Surface phase diagrams of CsI-T surface models

Figure 4 shows the SPDs for the considered surface reconstructions of the CsI-T surfaces (SPDs of PbI₂-T reconstructed models are given in Fig. S5 of the [supplementary material](#)). In principle, we need to plot the SPD in three dimensions (3D) because it depends on three chemical potentials: $\Delta\mu_{\text{Cs}}$, $\Delta\mu_{\text{Pb}}$, and $\Delta\mu_{\text{I}}$. Since such a 3D diagram

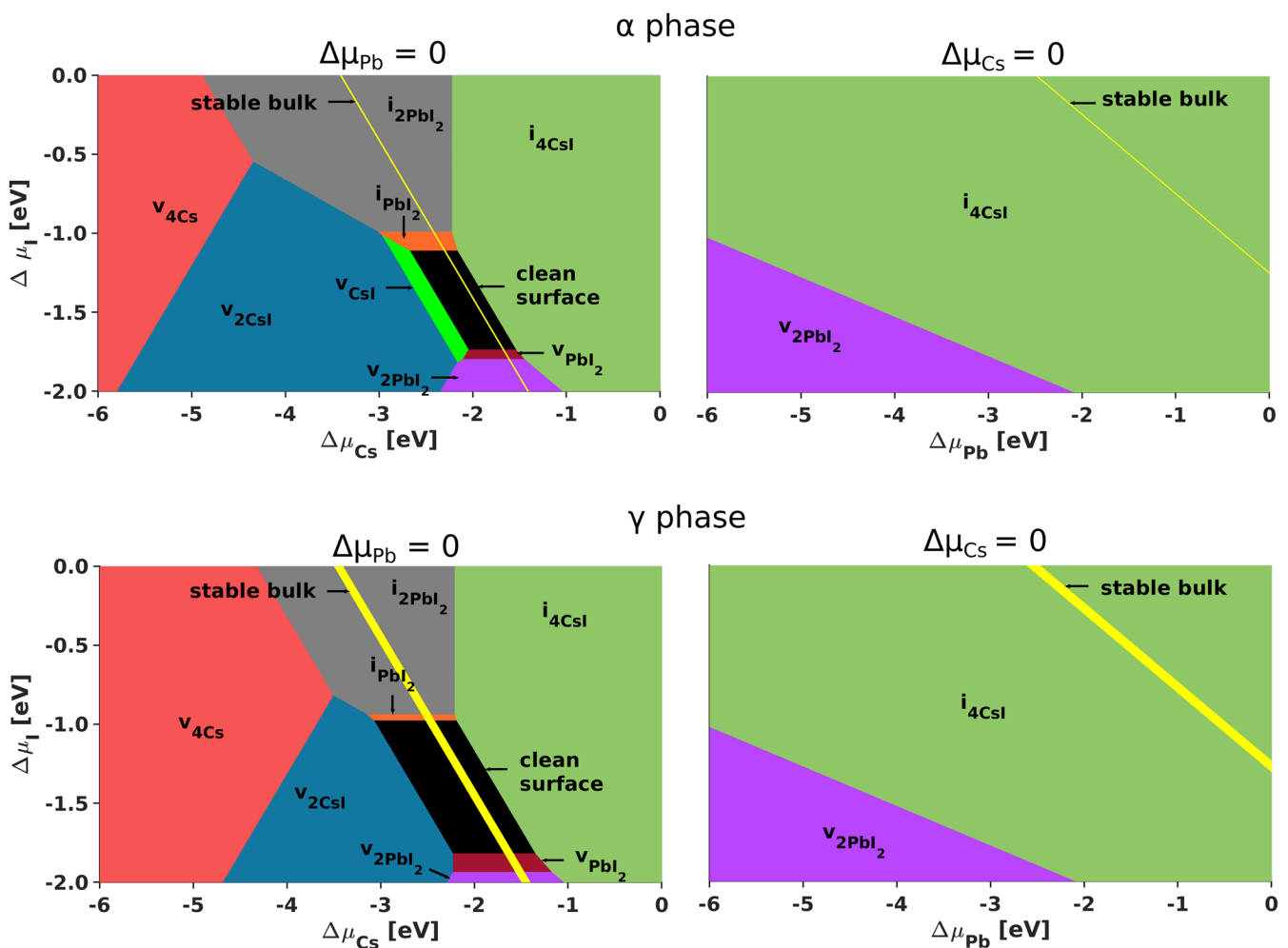


FIG. 4. Surface phase diagrams of reconstructed CsI-T surfaces with missing- and add-atoms as well as their complexes (upper panel for the α phase and lower panel for the γ phase). The yellow regions depict the thermodynamically stable range for the growth of bulk CsPbI₃.

is hard to visualize, we present two 2D slices instead, one $\Delta\mu_I/\Delta\mu_{Cs}$ slice at $\Delta\mu_{Pb} = 0$ and one $\Delta\mu_I/\Delta\mu_{Pb}$ slice at $\Delta\mu_{Cs} = 0$. The left side of Fig. 4 shows the SPDs at $\Delta\mu_{Pb} = 0$, and the right side shows $\Delta\mu_{Cs} = 0$. The vertical panels show the α and the γ phases, respectively. $\Delta\mu_I$ is plotted on the vertical axis, and the other chemical potential is plotted on the horizontal axis. The colored regions and their labels indicate the most stable surface at that pair of chemical potentials. The yellow shaded region again depicts the growth limit for stable bulk CsPbI₃, which serves as our reference to determine the most relevant surface models. We have also performed

reference calculations with the PBE functional⁷³ (see Fig. S1 of the supplementary material). The SPDs in PBE and PBEsol are almost identical, which demonstrates that PBEsol is appropriate for surface reconstructions.

For the α phase (Fig. 4 upper panel), we find the following stable surface structures at some point in the phase diagram in the Pb-rich limit ($\Delta\mu_{Pb} = 0$): v_{4Cs} , v_{CsI} , v_{2CsI} , v_{PbI_2} , v_{2PbI_2} , i_{4CsI} , i_{PbI_2} , i_{2PbI_2} , and the clean surface. In the Cs-rich limit ($\Delta\mu_{Cs} = 0$), we instead find v_{2PbI_2} and i_{4CsI} . The situation for the γ phase is very similar. The extent of some of the stability regions changes slightly from α to γ , and the

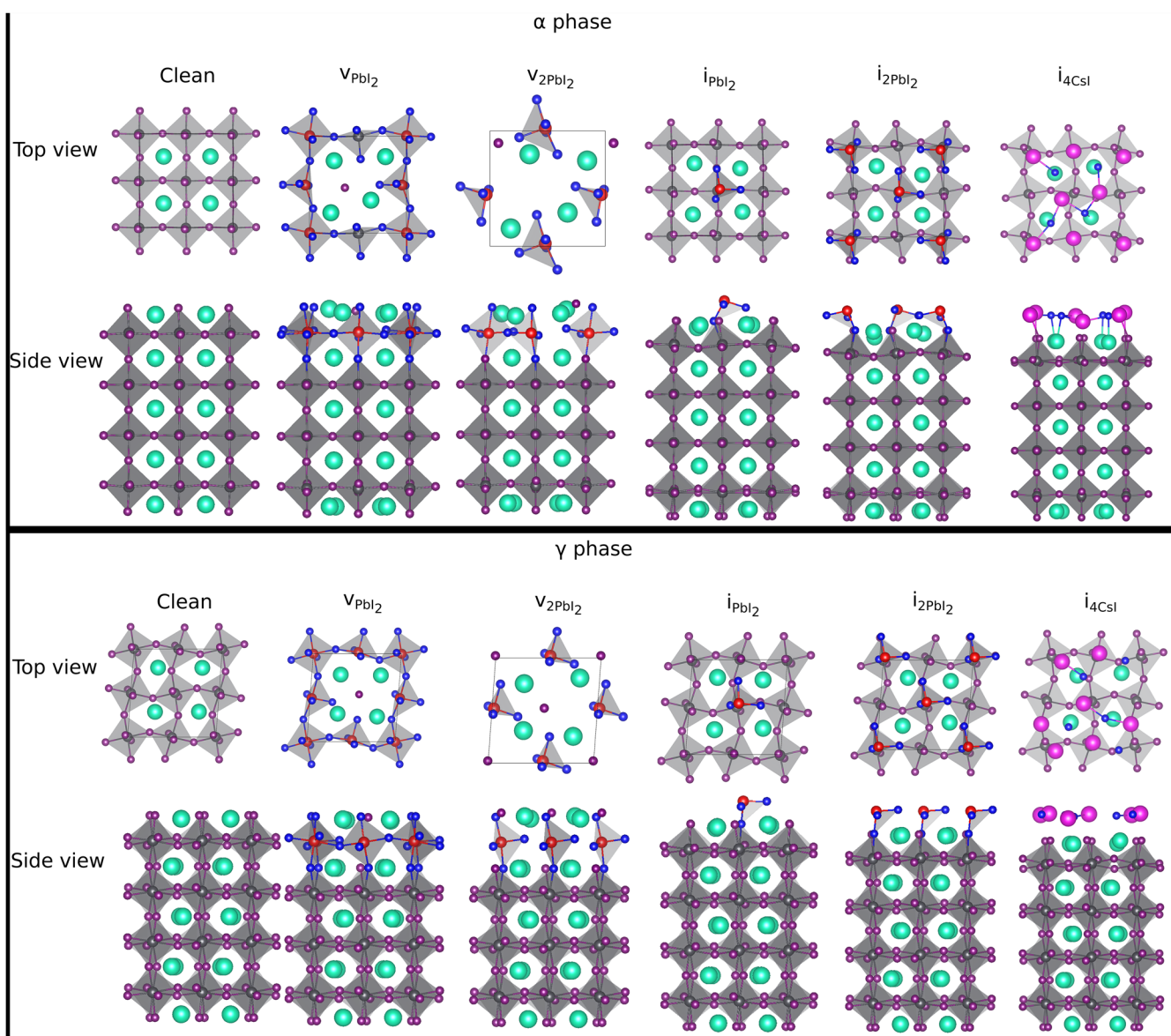


FIG. 5. Atomic structures of the most relevant surface reconstructions for the α phase (upper panel) and the γ phase (lower panel). The surface Pb and I atoms that exhibit pronounced displacements are highlighted by red and blue colors, respectively. The pink circles denote added Cs atoms.

v_{CsI} reconstruction disappears from the phase diagram (lower panel of Fig. 4).

With the exception of $v_{4\text{Cs}}$, all the observed reconstructions are valence-neutral, i.e., with addition or removal of valence-neutral units such as CsI or PbI_2 . Here, valence-neutral units refer to added or removed complexes that do not induce “net charges” on CsPbI_3 as a whole. The addition or removal of valence-neutral units is energetically more favorable than that of single atoms or non-valence-neutral complexes because it does not introduce free charge carriers, as we will demonstrate in Sec. III B. As expected, we observe Cs-deficient reconstructed models ($v_{4\text{Cs}}$, v_{CsI} , $v_{2\text{CsI}}$) for low $\Delta\mu_{\text{Cs}}$ and Cs-rich ones ($i_{4\text{CsI}}$) at the high $\Delta\mu_{\text{Cs}}$ region. A similar trend is observed for low and high Pb chemical potentials. A notable exception is the stability of $i_{4\text{CsI}}$ in the Pb-rich region in the upper right panel. Since the Cs chemical potential is at a maximum, the Cs-rich, $i_{4\text{CsI}}$ reconstruction dominates over Pb add-atom structures.

Of particular relevance to us are the surface reconstructions that intersect the bulk stability region (yellow region). These stable reconstructions that intersect the bulk region are the same for the α and the γ phases. In addition to the clean CsI -T surface, we find only the valence-neutral surface reconstructions $v_{2\text{PbI}_2}$, $v_{2\text{PbI}_2}$, i_{PbI_2} , $i_{2\text{PbI}_2}$, and $i_{4\text{CsI}}$. It is noteworthy that although the clean surface occupies quite a broad stability region for $\Delta\mu_{\text{Pb}} = 0$, it is only stable if the growth conditions are I-deficient and not at all in Cs-rich conditions.

2. Atomic structures of the most relevant surface reconstructions

Figure 5 shows the relaxed geometries of the most relevant surface models (clean, v_{PbI_2} , $v_{2\text{PbI}_2}$, i_{PbI_2} , $i_{2\text{PbI}_2}$, and $i_{4\text{CsI}}$) for the α and

the γ phases. The remaining surface structures are shown in Fig. S2. The clean surface does not exhibit any significant deviations from the bulk atomic positions after relaxation. Hence, all changes in the reconstructed structures will be discussed with reference to the clean surface hereafter.

In all reconstructions, we observe changes in the surface layer that translate into slight tilting of the surface octahedra. For instance, the surface octahedra in v_{PbI_2} for both phases tilt to account for the missing PbI_2 units. Similarly, the surface octahedra of i_{PbI_2} and $i_{2\text{PbI}_2}$ tilt to accommodate the added PbI_2 . In addition to the tilting, other slight changes in the atomic positions are observed. For example, the Cs–I bond lengths in the surfaces of $i_{4\text{CsI}}$ for both phases vary by ~ 0.1 Å. To highlight the changes in atomic positions, Cs, Pb, and I atoms of interest in Fig. 5 are depicted in pink, red and blue, respectively.

A more drastic change occurs for $v_{2\text{PbI}_2}$ in the α phase. The migration of I atoms within the surface layer leads to an asymmetric distribution of them, causing the formation of separate PbI_5 and PbI_4 polyhedra in the surface layer. This structure is similar to the findings of Haruyama *et al.* for MAPbI_3 ,^{42,43,74} in which they observed the formation of PbI_3 – PbI_5 polyhedra upon the removal of “one-half” of the PbI_2 units from the PbI_2 -T surfaces. Interestingly, we do not see the same atomic rearrangement for $v_{2\text{PbI}_2}$ in the γ phase. Instead, we find a relatively symmetric I distribution and two isolated PbI_4 polyhedra. The different behavior in the α phase is likely due to the larger lattice constant, which results in a larger Cs–Cs distance and a weaker binding of I atoms.

I migration is also observed in the $i_{2\text{I}}$ reconstruction of both phases and $v_{4\text{Cs}}$ of the γ phase (see Fig. S2 of the [supplementary material](#)). In each case, two I atoms move close to each other such

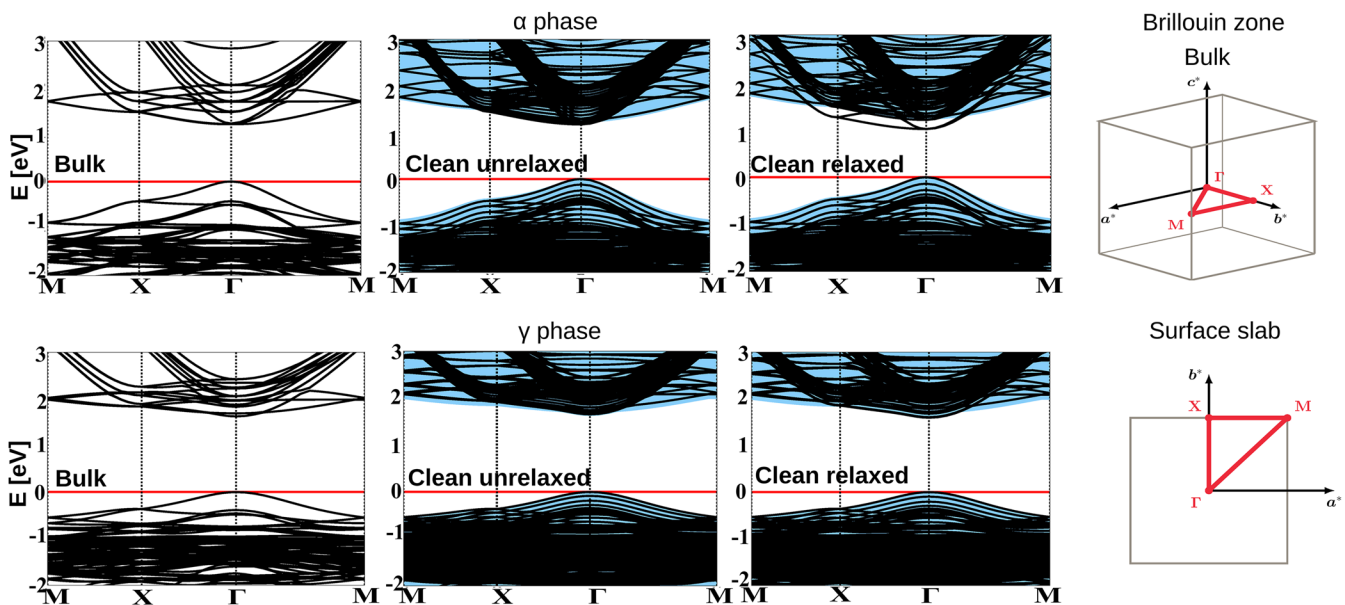


FIG. 6. Band structures of bulk CsPbI_3 and the clean surfaces (with and without geometry relaxation) in the α (upper panel) and γ (lower panel) phases. Both bulk and surface band structures are calculated with a 2×2 in-plane supercell to share a common Brillouin zone and k -point path. As shown in the Brillouin zone (far right), the in-plane k -point path for the bulk is the same as the surface. The VBM is set to 0, as marked by the red horizontal line. In the surface band structure plots, the projected bulk band structure is shown as blue shading.

that their distance is close to that of an I_2 molecule.⁷⁵ Specifically, the I–I distance in v_{4Cs} is reduced to ~ 2.9 Å. Similarly, the I–I distance of the added I atoms in i_{2I} reduces to ~ 2.9 Å in the α phase and ~ 2.8 Å in the γ phase. These values are close to the experimental bond length

(~ 2.67 Å) of the I_2 molecule in the gas phase,⁷⁵ albeit a bit larger since the surface I atoms are bound to other surface atoms such as Cs and Pb, thus reducing the bond strength of I–I. Experimentally, the formation of I_2 on the surface facilitates the degradation of

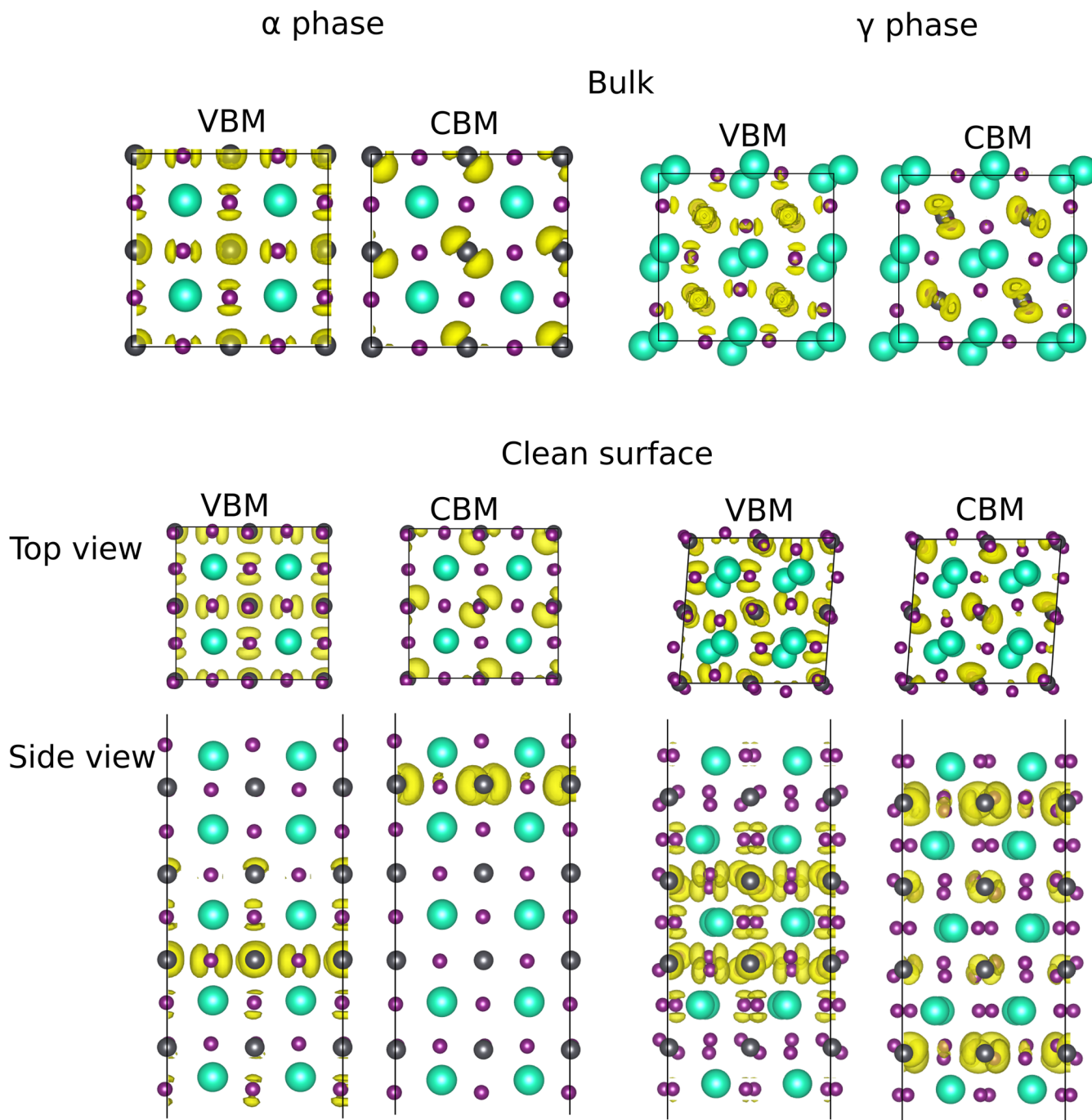


FIG. 7. Charge distribution of the VBM and CBM of bulk $CsPbI_3$ and the CsI -T clean surfaces for (a) the α and (b) the γ phase.

MAPbI₃ and FAPbI₃,^{76,77} while its effect on the stability of CsPbI₃ is yet unknown.

B. Electronic properties of most relevant CsI-T surfaces

In this section, we discuss the electronic properties of bulk CsPbI₃, the clean surfaces in the α and the γ phases, and the relevant reconstructions reported in Figs. 4 and 5.

1. Electronic properties of the bulk and the clean CsI-T surface

Figure 6 depicts the band structures of the bulk and the clean CsI-T surfaces of the α and the γ phases. For the bulk of both phases, we adopt the high-symmetry k -point path in the Brillouin zone for a simple-cubic lattice of the $2 \times 2 \times 2$ supercell model for simplicity. In addition, we only show the band structure along M–X– Γ –M with $M = (\frac{1}{2}, \frac{1}{2}, 0)$, $X = (0, \frac{1}{2}, 0)$, and $\Gamma = (0, 0, 0)$, i.e., within the a^*b^* plane of the Brillouin zone [identical to the $ab = (001)$ plane in real space in our cases]. Accordingly, we plot the band structure of the 2×2 surface unit cells of both phases along the same high-symmetry k -point path for an easy comparison. The valence band maximum (VBM) in all plots is set to zero. In the band structure plots of the surface models, the projected bulk band structure is included as a blue-shaded background to help identify possible surface states.^{78,79}

In both phases, bulk CsPbI₃ exhibits a direct bandgap at the Γ point. The charge densities (shown in Fig. 7) reveal that the VBM of CsPbI₃ in both phases is dominated by I-5p orbitals with a noticeable contribution from the Pb-6s orbitals, which gives rise to the well known antibonding character.^{42,43,53,80} The conduction band maximum (CBM) mainly consists of Pb-6p orbitals.

Next, we investigate if the CsI termination introduces surface states. The middle panels of Fig. 6 show the band structure of the two

unrelaxed CsI-T models. The bands of the supercell coincide with the projected bulk band structure, which indicates that no surface states appear. However, upon relaxation, the bottom of the conduction band is pulled into the bulk bandgap for the α phase but not for the γ phase, as can be seen in the right most band structure panels in Fig. 6. The clean surface of the α phase therefore exhibits a surface state that derives from the CsPbI₃ conduction band. This is further evidenced in Fig. 7, which shows that the lowest conduction band resides at the surface and has a Pb-6p character. In contrast, the corresponding state in the γ phase is quite clearly a bulk state and not a surface state.

2. Electronic properties of most relevant reconstructed CsI-T surface models

Figure 8 shows the band structures of the most relevant surface models observed in Fig. 4, i.e., v_{PbI_2} , $v_{2\text{PbI}_2}$, $i_{4\text{CsI}}$, i_{PbI_2} and $i_{2\text{PbI}_2}$. Similar to Fig. 6, the bulk band structure is included as the background for comparison.

Figure 8 displays a similar pattern as Fig. 6, i.e., the most notable changes in the band structure of the surface models appear for the α phase near the bottom of the conduction band. For neither phase, do we observe perturbations of the VBM region. Further inspection of the charge distributions of the valence-band-edge states shown in Fig. S3 of the supplementary material confirms that the VBM retains its bulk character for all relevant surface reconstructions.

For the reconstructed surface models of the α phase, we observe the same surface states as in the clean-surface model (Fig. 6). In addition, flat bands appear near or below the conduction band edge, which are most notable around the M-points of the band structure. The only exception is $i_{4\text{CsI}}$, for which the surface band structure strongly resembles that of the clean CsI-T surface. The flat bands are especially pronounced in the v_{PbI_2} and $v_{2\text{PbI}_2}$ models. Correspondingly, the states near the conduction band edge of these two surface reconstructions exhibit a more localized character than for the clean

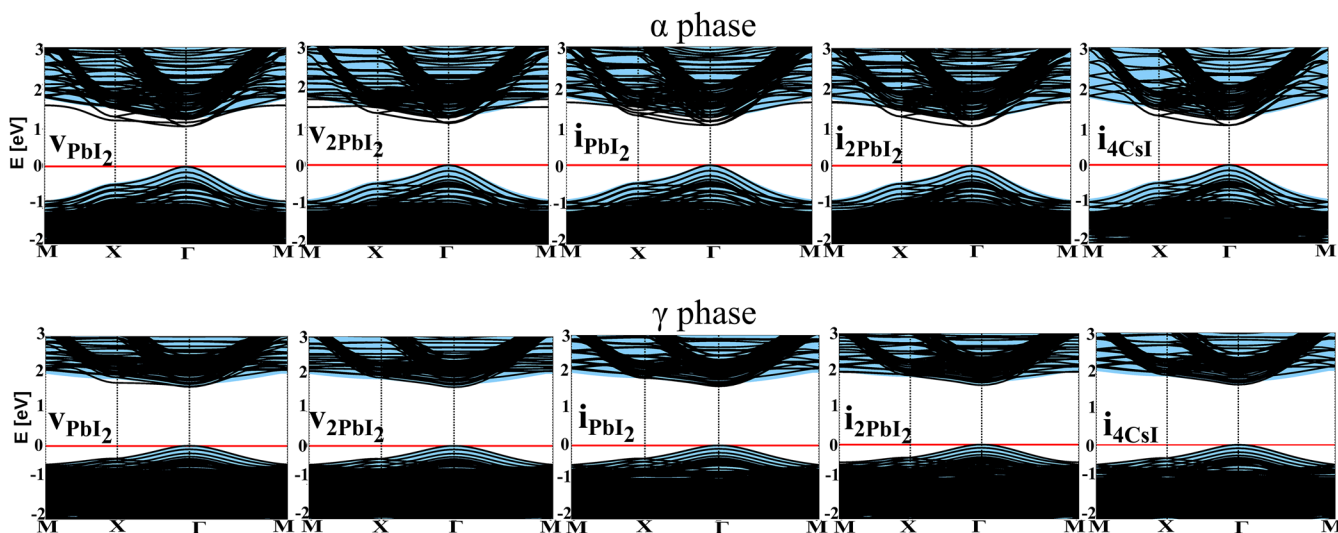


FIG. 8. Band structures of the most relevant reconstructed CsI-T surface models in the α and the γ phases. The legends follow Fig. 6.

surface (compare the upper panel of Fig. S3 of the [supplementary material](#) with Fig. 7). For these surface models, the reconstruction therefore introduces additional surface states to the ones of the clean surface.

IV. DISCUSSION

Our results offer guidance for growing favorable CsPbI₃ surfaces. By favorable, we here imply surface reconstructions that have a bulk-like band structure and no additional states in the bandgap or perturbations of the band edges that might adversely affect the transport properties. Our analysis of Sec. III B 2 suggests that the γ phase of CsPbI₃ is generally more suited for this purpose, as all of its stable surface reconstructions are free of band edge perturbations.

For the α phase, the objective would be to avoid both PbI₂ deficient (v_{PbI_2} and $v_{2\text{PbI}_2}$) and rich (i_{PbI_2} and $i_{2\text{PbI}_2}$) reconstructions. Fortunately, the clean surface is stable across a wide range of the bulk stability region, as our surface phase diagram analysis shows. For Cs rich growth conditions, the $i_{4\text{CsI}}$ phase dominates the phase diagram. This phase provides a good alternative to the clean surface since its band structure resembles that of the clean surface closely.

V. CONCLUSIONS

In summary, we have studied the surface atomic and electronic structure of CsPbI₃ from first-principles. For both the α (cubic) and the γ (orthorhombic) phases, we have considered the clean-surface models and a series of surface reconstructions. Surface phase diagram analysis indicates that the CsI-terminated (001) surface is more stable within a large range of allowed chemical potentials for both phases. In addition, several CsI and PbI₂ rich and deficient surface reconstructions are stable. These surface reconstructions do not induce deep energy levels in the bandgap. Nevertheless, the removal of PbI₂ units in the CsI-terminated α -CsPbI₃ surface has noticeable effects on the material's electronic structure, especially close to the conduction band edge. Combining our surface-phase diagram and electronic structure analysis allows us to recommend growth regimes for CsPbI₃ surfaces with favorable transport properties. Our work highlights the complexity of CsPbI₃ surfaces and provides avenues for future surface science and interface studies.

SUPPLEMENTARY MATERIAL

See the [supplementary material](#) for CsI-T SPDs computed with PBE, charge density plots of all relevant surface models with CsI-termination, surface phase diagrams of PbI₂-terminated models, crystal structures of studied surface models in both CsI-T and PbI₂-T (that are not included in the main text), the formation energies of all surface models, and the evaluation of the effect of spin-orbit coupling.

ACKNOWLEDGMENTS

We acknowledge the computing resources by the CSC-IT Center for Science, the Aalto Science-IT project, and Xi'an Jiaotong

University's HPC Platform. An award of computer time was provided by the Innovative and Novel Computational Impact on Theory and Experiment (INCITE) program. This research used resources of the Argonne Leadership Computing Facility, which is a DOE Office of Science User Facility supported under Contract No. DE-AC02-06CH11357. We further acknowledge funding from the European Union's Horizon 2020 research and innovation program under Grant Agreement No. 676580 [The Novel Materials Discovery (NOMAD) Laboratory], the Väisälä Foundation as well as the Academy of Finland through its Centres of Excellence Programme (Grant No. 284621), its key project funding scheme (Grant No. 305632), and Project No. 316347.

DATA AVAILABILITY

The data that support the findings of this study are openly available in the Novel Materials Discovery (NOMAD) repository.⁷⁰

REFERENCES

- 1 National Renewable Energy Laboratory: Best research-cell efficiencies, <https://www.nrel.gov/pv/assets/pdfs/best-research-cell-efficiencies.20200311.pdf>, 2020.
- 2 H.-S. Kim, C.-R. Lee, J.-H. Im, K.-B. Lee, T. Moehl, A. Marchioro, S.-J. Moon, R. Humphry-Baker, J.-H. Yum, J. E. Moser *et al.*, *Sci. Rep.* **2**, 591 (2012).
- 3 M. M. Lee, J. Teuscher, T. Miyasaka, T. N. Murakami, and H. J. Snaith, *Science* **338**, 643 (2012).
- 4 L.-Y. Huang and W. R. L. Lambrecht, *Phys. Rev. B* **90**, 195201 (2014).
- 5 Q. Lin, A. Armin, D. M. Lyons, P. L. Burn, and P. Meredith, *Adv. Mater.* **27**, 2060 (2015).
- 6 H. Cho, S.-H. Jeong, M.-H. Park, Y.-H. Kim, C. Wolf, C.-L. Lee, J. H. Heo, A. Sadhanala, N. Myoung, S. Yoo *et al.*, *Science* **350**, 1222 (2015).
- 7 H. J. Snaith, *J. Phys. Chem. Lett.* **4**, 3623 (2013).
- 8 M. A. Green, A. Ho-Baillie, and H. J. Snaith, *Nat. Photon.* **8**, 506 (2014).
- 9 S. D. Stranks, G. E. Eperon, G. Grancini, C. Menelaou, M. J. P. Alcocer, T. Leijtens, L. M. Herz, A. Petrozza, and H. J. Snaith, *Science* **342**, 341 (2013).
- 10 G. Xing, N. Mathews, S. Sun, S. S. Lim, Y. M. Lam, M. Grätzel, S. Mhaisalkar, and T. C. Sum, *Science* **342**, 344 (2013).
- 11 G. E. Eperon, G. M. Paternò, R. J. Sutton, A. Zampetti, A. A. Haghighirad, F. Cacialli, and H. J. Snaith, *J. Mater. Chem. A* **3**, 19688 (2015).
- 12 J. Troughton, K. Hooper, and T. M. Watson, *Nano Energy* **39**, 60 (2017).
- 13 G. Niu, W. Li, F. Meng, L. Wang, H. Dong, and Y. Qiu, *J. Mater. Chem. A* **2**, 705 (2014).
- 14 G. Niu, X. Guo, and L. Wang, *J. Mater. Chem. A* **3**, 8970 (2015).
- 15 J. Huang, S. Tan, P. D. Lund, and H. Zhou, *Energy Environ. Sci.* **10**, 2284 (2017).
- 16 G.-H. Kim, H. Jang, Y. J. Yoon, J. Jeong, S. Y. Park, B. Walker, I.-Y. Jeon, Y. Jo, H. Yoon, M. Kim *et al.*, *Nano Lett.* **17**, 6385 (2017).
- 17 I. Mesquita, L. Andrade, and A. Mendes, *Renewable Sustainable Energy Rev.* **82**, 2471 (2018).
- 18 A. Cicciooli and A. Latini, *J. Phys. Chem. Lett.* **9**, 3756 (2018).
- 19 F. Li, J. Yuan, X. Ling, Y. Zhang, Y. Yang, S. H. Cheung, C. H. Y. Ho, X. Gao, and W. Ma, *Adv. Funct. Mater.* **28**, 1706377 (2018).
- 20 L. C. Schmidt, A. Pertegás, S. González-Carrero, O. Malinkiewicz, S. Agouram, G. M. Espallargas, H. J. Bolink, R. E. Galian, and J. Pérez-Prieto, *J. Am. Chem. Soc.* **136**, 850 (2014).
- 21 S. González-Carrero, R. E. Galian, and J. Pérez-Prieto, *J. Mater. Chem. A* **3**, 9187 (2015).
- 22 H. Dong, J. Xi, L. Zuo, J. Li, Y. Yang, D. Wang, Y. Yu, L. Ma, C. Ran, W. Gao *et al.*, *Adv. Funct. Mater.* **29**, 1808119 (2019).
- 23 L. N. Quan, M. Yuan, R. Comin, O. Voznyy, E. M. Bearegard, S. Hoogland, A. Buin, A. R. Kirmani, K. Zhao, A. Amassian *et al.*, *J. Am. Chem. Soc.* **138**, 2649 (2016).

- ²⁴L. Dou, *J. Mater. Chem. C* **5**, 11165 (2017).
- ²⁵C. Ran, J. Xi, W. Gao, F. Yuan, T. Lei, B. Jiao, X. Hou, and Z. Wu, *ACS Energy Lett.* **3**, 713 (2018).
- ²⁶Z. Wang, A. M. Ganose, C. Niu, and D. O. Scanlon, *J. Mater. Chem. A* **6**, 5652 (2018).
- ²⁷C. Liu, W. Huhn, K.-Z. Du, A. Vazquez-Mayagoitia, D. Dirkes, W. You, Y. Kanai, D. B. Mitzi, and V. Blum, *Phys. Rev. Lett.* **121**, 146401 (2018).
- ²⁸C. Ran, W. Gao, J. Li, J. Xi, L. Li, J. Dai, Y. Yang, X. Gao, H. Dong, B. Jiao *et al.*, *Joule* **3**, 3072 (2019).
- ²⁹F. Matteocci, L. Cinà, E. Lamanna, S. Cacovich, G. Divitini, P. A. Midgley, C. Ducati, and A. di Carlo, *Nano Energy* **30**, 162 (2016).
- ³⁰R. Cheacharoen, N. Rolston, D. Harwood, K. A. Bush, R. H. Dauskardt, and M. D. McGehee, *Energy Environ. Sci.* **11**, 144 (2018).
- ³¹R. Cheacharoen, C. C. Boyd, G. F. Burkhard, T. Leijtens, J. A. Raiford, K. A. Bush, S. F. Bent, and M. D. McGehee, *Sustain. Energy Fuels* **2**, 2398 (2018).
- ³²A. Seidu, L. Himanen, J. Li, and P. Rinke, *New J. Phys.* **21**, 083018 (2019).
- ³³J. H. Noh, S. H. Im, J. H. Heo, T. N. Mandal, and S. I. Seok, *Nano Lett.* **13**, 1764 (2013).
- ³⁴C. Yi, J. Luo, S. Meloni, A. Boziki, N. Ashari-Astani, C. Grätzel, S. M. Zakeeruddin, U. Röthlisberger, and M. Grätzel, *Energy Environ. Sci.* **9**, 656 (2016).
- ³⁵Y. Zhou, Z. Zhou, M. Chen, Y. Zong, J. Huang, S. Pang, and N. P. Pature, *J. Mater. Chem. A* **4**, 17623 (2016).
- ³⁶H. Tan, A. Jain, O. Voznyy, X. Lan, F. P. G. de Arquer, J. Z. Fan, R. Quintero-Bermudez, M. Yuan, B. Zhang, Y. Zhao *et al.*, *Science* **355**, 722 (2017).
- ³⁷W. Gao, C. Ran, J. Li, H. Dong, B. Jiao, L. Zhang, X. Lan, and X. Hou, Z. Wu, *J. Phys. Chem. Lett.* **9**, 6999 (2018).
- ³⁸J.-P. Correa-Baena, A. Abate, M. Saliba, W. Tress, T. J. Jacobsson, M. Grätzel, and A. Hagfeldt, *Energy Environ. Sci.* **10**, 710 (2017).
- ³⁹A. M. Ganose, C. N. Savory, and D. O. Scanlon, *Chem. Commun.* **53**, 20 (2017).
- ⁴⁰L. A. Frolova, D. V. Anokhin, A. A. Piryazev, S. Y. Luchkin, N. N. Dremova, K. J. Stevenson, and P. A. Troshin, *J. Phys. Chem. Lett.* **8**, 67 (2017).
- ⁴¹Y. Wang, M. I. Dar, L. K. Ono, T. Zhang, M. Kan, Y. Li, L. Zhang, X. Wang, Y. Yang, X. Gao *et al.*, *Science* **365**, 591 (2019).
- ⁴²J. Haruyama, K. Sodeyama, L. Han, and Y. Tateyama, *J. Phys. Chem. Lett.* **5**, 2903 (2014).
- ⁴³J. Haruyama, K. Sodeyama, L. Han, and Y. Tateyama, *Acc. Chem. Res.* **49**, 554 (2016).
- ⁴⁴O. Grånäs, D. Vinichenko, and E. Kaxiras, *Sci. Rep.* **6**, 36108 (2016).
- ⁴⁵A. Akbari, J. Hashemi, E. Mosconi, F. De Angelis, and M. Hakala, *J. Mater. Chem. A* **5**, 2339 (2017).
- ⁴⁶Q. Jiang, Y. Zhao, X. Zhang, X. Yang, Y. Chen, Z. Chu, Q. Ye, X. Li, Z. Yin, and J. You, *Nat. Photon.* **13**, 460 (2019).
- ⁴⁷P. Chen, Y. Bai, S. Wang, M. Lyu, J.-H. Yun, and L. Wang, *Adv. Funct. Mater.* **28**, 1706923 (2018).
- ⁴⁸Y. Cho, A. M. Soufiani, J. S. Yun, J. Kim, D. S. Lee, J. Seidel, X. Deng, M. A. Green, S. Huang, and A. W. Y. Ho-Baillie, *Adv. Energy Mater.* **8**, 1703392 (2018).
- ⁴⁹M. Saliba, T. Matsui, J.-Y. Seo, K. Domanski, J.-P. Correa-Baena, M. K. Nazeeruddin, S. M. Zakeeruddin, W. Tress, A. Abate, A. Hagfeldt *et al.*, *Energy Environ. Sci.* **9**, 1989 (2016).
- ⁵⁰M. Saliba, S. Orlandi, T. Matsui, S. Aghazada, M. Cavazzini, J.-P. Correa-Baena, P. Gao, R. Scopelliti, E. Mosconi, K.-H. Dahmen *et al.*, *Nat. Energy* **1**, 15017 (2016).
- ⁵¹M. Saliba, T. Matsui, K. Domanski, J.-Y. Seo, A. Ummadisingu, S. M. Zakeeruddin, J.-P. Correa-Baena, W. R. Tress, A. Abate, A. Hagfeldt *et al.*, *Science* **354**, 206 (2016).
- ⁵²Y. Li, C. Zhang, D. Huang, Q. Shen, Y. Cheng, and W. Huang, *Appl. Phys. Lett.* **111**, 162106 (2017).
- ⁵³Y. Huang, W.-J. Yin, and Y. He, *J. Phys. Chem. C* **122**, 1345 (2018).
- ⁵⁴R. J. Sutton, M. R. Filip, A. A. Haghighirad, N. Sakai, B. Wenger, F. Giustino, and H. J. Snaith, *ACS Energy Lett.* **3**, 1787 (2018).
- ⁵⁵R. A. Evarestov, A. Senocrate, E. A. Kotomin, and J. Maier, *Phys. Chem. Chem. Phys.* **21**, 7841 (2019).
- ⁵⁶K. Reuter and M. Scheffler, *Phys. Rev. Lett.* **90**, 046103 (2003).
- ⁵⁷K. Reuter and C. Stampfl, and M. Scheffler, in *Handbook of Material Modeling*, edited by S. Yip (Springer Dordrecht, 2005).
- ⁵⁸K. Reuter and M. Scheffler, *Phys. Rev. B* **68**, 045407 (2003).
- ⁵⁹J. P. Perdew, A. Ruzsinszky, G. I. Csonka, O. A. Vydrov, G. E. Scuseria, L. A. Constantin, X. Zhou, and K. Burke, *Phys. Rev. Lett.* **100**, 136406 (2008).
- ⁶⁰V. Blum, R. Gehrke, F. Hanke, P. Havu, V. Havu, X. Ren, K. Reuter, and M. Scheffler, *Comput. Phys. Commun.* **180**, 2175 (2009).
- ⁶¹V. Havu, V. Blum, P. Havu, and M. Scheffler, *J. Comput. Phys.* **228**, 8367 (2009).
- ⁶²S. V. Levchenko, X. Ren, J. Wierfink, R. Johanni, P. Rinke, V. Blum, and M. Scheffler, *Comput. Phys. Commun.* **192**, 60 (2015).
- ⁶³R. X. Yang, J. M. Skelton, E. L. da Silva, J. M. Frost, and A. Walsh, *J. Phys. Chem. Lett.* **8**, 4720 (2017).
- ⁶⁴M. Bokdam, J. Lahnsteiner, B. Ramberger, T. Schäfer, and G. Kresse, *Phys. Rev. Lett.* **119**, 145501 (2017).
- ⁶⁵E. van Lenthe, E. J. Baerends, and J. G. Snijders, *J. Chem. Phys.* **99**, 4597 (1993).
- ⁶⁶F. Knuth, C. Carbogno, V. Atalla, V. Blum, and M. Scheffler, *Comput. Phys. Commun.* **190**, 33 (2015).
- ⁶⁷J. Neugebauer and M. Scheffler, *Phys. Rev. B* **46**, 16067 (1992).
- ⁶⁸P. Schulz, D. Cahen, and A. Kahn, *Chem. Rev.* **119**, 3349 (2019).
- ⁶⁹L. Himanen, A. Geurts, A. S. Foster, and P. Rinke, *Adv. Sci.* **6**, 1900808 (2019).
- ⁷⁰Novel Materials Discovery (NOMAD) repository, <https://doi.org/10.17172/NOMAD/2021.01.28-1>.
- ⁷¹W.-J. Yin, T. Shi, and Y. Yan, *Appl. Phys. Lett.* **104**, 063903 (2014).
- ⁷²W. Geng, C.-J. Tong, Z.-K. Tang, C. Yam, Y.-N. Zhang, W.-M. Lau, and L.-M. Liu, *J. Materiomics* **1**, 213 (2015).
- ⁷³J. P. Perdew, K. Burke, and M. Ernzerhof, *Phys. Rev. Lett.* **77**, 3865 (1996).
- ⁷⁴J. Haruyama, K. Sodeyama, L. Han, and Y. Tateyama, *J. Am. Chem. Soc.* **137**, 10048 (2015).
- ⁷⁵L. V. Gurvich, I. V. Veyts, and C. B. Alcock, *Thermodynamic Properties of Individual Substances* (Hemisphere Publishing Co., New York, 1989).
- ⁷⁶S. Wang, Y. Jiang, E. J. Juarez-Perez, L. K. Ono, and Y. Qi, *Nat. Energy* **2**, 16195 (2017).
- ⁷⁷F. Fu, S. Pisoni, Q. Jeangros, J. Sastre-Pellicer, M. Kawecki, A. Paracchino, T. Moser, J. Werner, C. Andres, L. Duchêne *et al.*, *Energy Environ. Sci.* **12**, 3074 (2019).
- ⁷⁸J. E. Ingersfield, *Rep. Prog. Phys.* **45**, 223 (1982).
- ⁷⁹N. J. Speer, M. K. Brinkley, Y. Liu, C. M. Wei, T. Miller, and T.-C. Chiang, *Europhys. Lett.* **88**, 67004 (2009).
- ⁸⁰W. Li, J. Liu, F.-Q. Bai, H.-X. Zhang, and O. V. Prezhdo, *ACS Energy Lett.* **2**, 1270 (2017).